Article

Effects of Lead Iodide Crystallization on Photovoltaic Performance of Perovskite Solar Cells by the Vapor-Solid Reaction Method

Qin Zou, Guoyuan Zheng,* Disheng Yao, Jilin Wang, Nan Tian, Shuyi Mo, and Fei Long*

Read Online

ACCESS | Metrics & More | Article Recommendations | SI Supporting Information

ABSTRACT: The vapor-solid reaction method (VRM) is one of the promising techniques to prepare high-performance perovskite solar cells. Herein, PbI_2 precursor films were prepared by vacuum evaporation. It was found that the PbI_2 precursor films exhibit high crystallinity and orderly morphology at the substrate temperature of 110 °C. On this basis, the precursor films were prepared by VRM to obtain high-quality perovskite films and the power conversion efficiency (PCE) of perovskite solar cells (PSCs) devices reached 17.1%. In contrast, the PbI_2 film precursor was prepared on the substrate without being heated and the PCE of the final PSCs devices was only 13.04%.
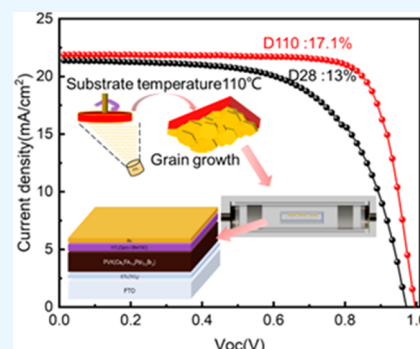
1. INTRODUCTION

Hybrid metal halide perovskite has become one of the most promising photovoltaic materials due to its excellent optical absorption coefficient, high carrier mobility, and adjustable band gap.[1−4] At present, the power conversion efficiency (PCE) of perovskite solar cells (PSCs) recorded by the National Renewable Energy Laboratory (NREL) has reached 25.7%.[5] However, most studies on PSCs are based on the fabrication of small-area devices with one-step or sequential two-step solution-processed methods.[6−8] In order to obtain high-quality perovskite films, efforts have been made to surface modification strategies, such as solvent engineering, anti-solvent-assisted crystallization, and vapor-assisted nucleation.[9−15] These methods require the use of toxic organic solvents such as chlorobenzene (CB), dimethylformamide (DMF), and dimethyl sulfoxide (DMSO),[16,17] which raise the risks of environment and health in mass production. Therefore, it is worth exploring the method of developing simple, non-toxic solvent, and easy-to-prepare efficient large-area PSCs.

In recent years, other deposition technologies have also been widely used to prepare high-quality perovskite films.[18] Vapor-solid reaction method (VRM) technology can effectively solve the problem of using toxic solvents and large-scale preparation. The technology of preparing perovskite thin films by VRM is that MAI/FAI gas molecules diffuse and react in the PbI_2 precursor layer to form perovskite. This method has the advantages of high surface coverage, low surface roughness, good compatibility with large area equipment, and accurate control of film thickness.[19−21] In fact, researchers have mainly adopted improved evaporation methods[22−25] and component engineering[26−29] to improve the quality of perovskite films and have made encouraging progress. However, there are few

reports about the effect of the quality of PbI_2 precursor films on the properties of perovskite. In this work, the perovskite layer was prepared by VRM technology. We take improving the crystallization of the PbI_2 precursor as the basis for preparing high-quality perovskite films. This study enriches the growth mechanism of the perovskite thin film in the field of VRM technology and provides a reference for exploring high-performance PSCs.

2. EXPERIMENTAL DETAILS

2.1. Materials. All reagents were used as is without further purification. The following were used for the experiment: titanium tetrachloride (TiCl$_4$, 99.5% Aladdin), methamidine hydroiodate (FAI, 99.9%, preferred), cesium bromide (CsBr, 99.99%, Paulet), lead iodide (PbI$_2$, 99.99%, Paulet), isopropyl alcohol (IPA, >99.7%, Siluron), Spiro-OMeTAD (99.86%, preferred), CB (dehydrating >99.9%, preferred), bis-(trifluoromethyl sulfonyl) Li-imide (Li-TFSI, 99%, Meryl), 4-*tert*-butylpyridine (*t*BP, 99.9%, preferred), acetonitrile (CAN, dehydrating >99.9%, preferred).

2.2. Preparation of the TiO$_2$/FTO Structure (ETL). First, a 2 cm × 1.5 cm FTO glass substrate was cleaned with acetone, deionized water, and 95% ethanol solution successively for 20 min under ultrasonic conditions. Then, it was dried and set
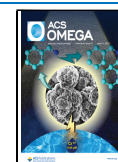
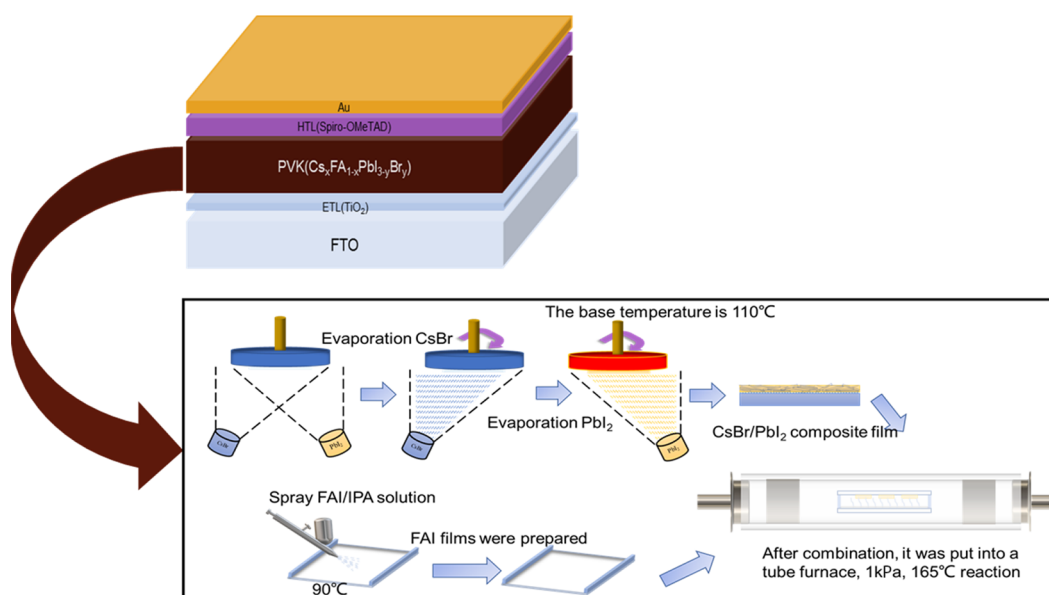**Figure 1.** Structure of PSC and schematic diagram of the two-step vapor deposition process of the $Cs_xFA_{1-x}PbI_{3-y}Br_y$ perovskite film.

aside. Before the next step, a 0.5 cm heat-resistant tape was attached to the edge of the substrate. The TiO_2/FTO substrate preparation process is as follows: The solution was measured with the volume ratio of $TiCl_4$:ultra-pure water =1:3, and the $TiCl_4$ solution was added into ultra-pure water (ice bath) in small amounts many times and stirred strongly for 30 min, and then TiO_2 precursor mother liquor was prepared and stored in the refrigerator. The prepared mother liquor was diluted again, and then the FTO glass was soaked in it, put in a drying oven, and kept at 70 °C for 40 min. The soaked FTO glass was washed and blow-dried, and the heat-resistant tape was removed. Finally, the substrate was kept in a muffle furnace at 450 °C for 2 h and the TiO_2/FTO substrate was obtained after cooling.

2.3. Preparation of $Cs_xFA_{1-x}PbI_{3-y}Br_y$/TiO$_2$/FTO (Perovskite). TiO_2/FTO was put into the vacuum evaporation chamber, the 30 nm CsBr film was evaporated at the condition of 6×10^{-6} Pa at the rate of about 0.3 Å/s, and the CsBr/TiO_2/FTO substrate was obtained. The CsBr/TiO_2/FTO substrate was heated to 28, 90, 110, and 130 °C, the PbI_2 film was prepared at the evaporation rate of 4 Å/s, and the precursor of PbI_2/CsBr/TiO_2/FTO was prepared.

112.5 mg of FAI was dissolved in 5 mL of IPA solvent and sprayed on a glass substrate at 90 °C. The PbI_2/CsBr/TiO_2/FTO precursor was inverted on the glass and then transferred to a tubular furnace. The tubular furnace was heated to 165 °C under a vacuum condition of 1 kPa for 20 min. Finally, the samples were removed from the tube furnace and heat-treated at 170 °C for 10 min to obtain $Cs_xFA_{1-x}PbI_{3-y}Br_y$/TiO$_2$/FTO thin films. The deposition process of the $Cs_xFA_{1-x}PbI_{3-y}Br_y$ perovskite film is shown in Figure 1.

2.4. Preparation of the Au/Spiro-OMeTAD/ $Cs_xFA_{1-x}PbI_{3-y}Br_y$/TiO$_2$/FTO Device. As precursors to the Spiro-OMeTAD hole transport layer (HTL), 72.5 mg of Spiro-OMeTAD, 1 mL of CB, 18 μL of Li-TFSI, and 29 μL of tBP were mixed. The solution of Li-TFSI was prepared by dissolving 52 mg of Li-TFSI powder in 0.1 mL of ACN solvent. The precursor solution was spun onto the $Cs_xFA_{1-x}PbI_{3-y}Br_y$/TiO$_2$/FTO structure at a speed of 3000 rpm for 30 s. The thickness of the HTL was about 200 nm.

The entire Spiro-OMeTAD film was prepared in a nitrogen glove box. The Spiro-OMeTAD/$Cs_xFA_{1-x}PbI_{3-y}Br_y$/TiO$_2$/FTO structure was transferred to the evaporation chamber. A gold electrode of about 80 nm was prepared under vacuum conditions of 6×10^{-4} Pa with an evaporation rate of 0.5 Å/s. Finally, the structure of a Au/Spiro-OMeTAD/$Cs_xFA_{1-x}PbI_{3-y}Br_y$/TiO$_2$/FTO solar cell device was obtained.

2.5. Performance Measurement. The morphology of samples was observed by field emission scanning electron microscopy (FESEM, Hitachi S-4800). The phase composition and the crystal structure were identified by the X-ray diffraction (XRD) method (PANalytical, X'Pert Pro MRD). The absorption and transmission spectra of films were measured using a UV−visible/near-infrared spectrophotometer (UV-3600, Shimadzu, China) in the wavelength range of 300 to 820 nm. The photoluminescence (PL) spectra of the films were measured by a fluorescence spectrophotometer (HORIBA, QuantaMaster 8000). Time-resolved photoluminescence (TR-PL) spectra were measured using the FLS-1000 system. Space-charge-limited current (SCLC) measurement was carried out by a Keithley 2400 source meter. The performance of the device was measured by the solar cell measurement system under illumination conditions (AM 1.5G) of 100 mW/cm^2 (Newport, USA). External quantum efficiency (EQE) spectra were collected in DC mode by a monochromatic incident photon-to-electron conversion efficiency (IPCE) system (Solar Cell Scan 100, Zolix Instruments Co., Ltd.).

3. RESULTS AND DISCUSSION

The perovskite samples prepared from CsBr/PbI_2 precursor films deposited at different substrate temperatures were named P28, P90, P110, and P130, and their corresponding devices were named D28, D90, D110, and D130, respectively.

The substrate temperature had a great influence on the morphology of PbI_2 thin films prepared by thermal evaporation. As shown in Figure 2a, the PbI_2 that was deposited at 28 °C showed a rough and loose surface with many holes and relatively small grain size. However, as shown in Figure 2b, the PbI_2 at 110 °C was smooth and compact with
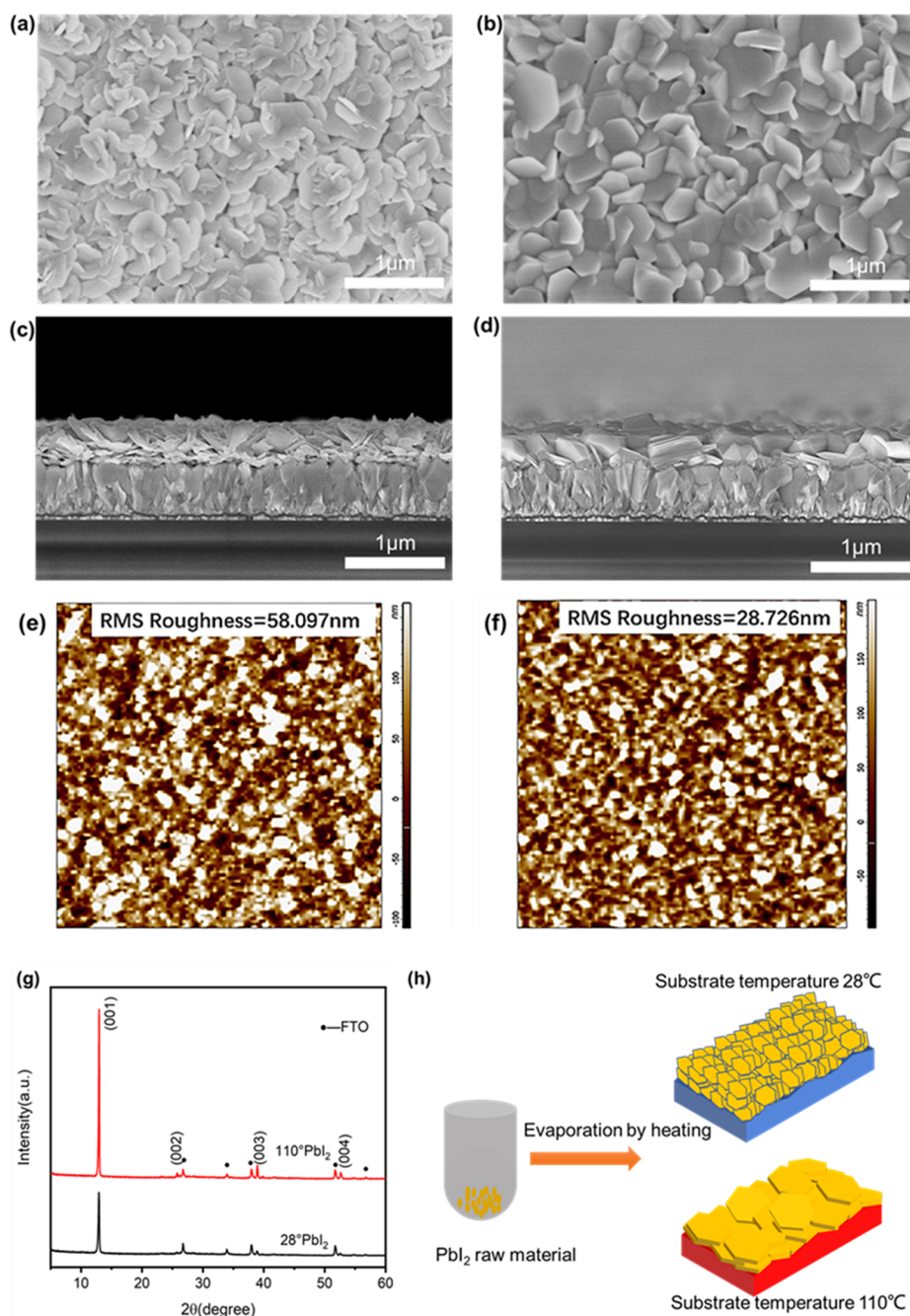
Figure 2. Top-view SEM images of the surface morphology of PbI$_2$ films at substrate temperatures of 28 °C (a) and 110 °C (b), respectively. Cross-sectional-view SEM images of the surface morphology of PbI$_2$ films at substrate temperatures of 28 °C (c) and 110 °C (d), respectively. AFM morphologies of CsBr/PbI$_2$ films deposited at (e) 28 °C and (f) 110 °C, respectively. RMS (root means square) roughness is shown in each case. (g) The XRD patterns of PbI$_2$ films were prepared at 28 and 110 °C, respectively. (h) Crystallization diagram of PbI$_2$ at 28 and 110 °C, respectively.

significantly fewer pores and produced larger grains. This is consistent with the grain size distribution diagram of PbI$_2$ shown in Figure S2. Figure 2c,d shows the cross sections of the PbI$_2$ layer at substrate temperatures of 28 and 110 °C, respectively. It is observed that the PbI$_2$ layer deposited at low temperature was an irregular flake and there were obvious gaps and holes at the junction with the substrate. When the substrate temperature increased to 110 °C, the PbI$_2$ layer was thick and dense with a tight binding to the substrate. In addition, it is obviously observed in Figure S1 that when the substrate temperature increased to 130 °C, the thickness of

PbI$_2$ decreased significantly. In addition, when the substrate temperature was 90 °C, the PbI$_2$ layer still had obvious holes similar to the 28 °C structure. The morphology of the PbI$_2$ films was further investigated by atomic force microscopy (AFM). As shown in Figure 2e,f, the surface roughness of the sample decreased from 58.097 to 28.726 nm when the substrate temperature increased from 28 to 110 °C.

The crystallization of PbI$_2$ was evaluated by XRD. As shown in Figure 2g, the diffraction peaks at 12.69, 25.55, 38.71, and 52.45° correspond to the (001), (002), (003), and (004) lattice planes of PbI$_2$,[30] respectively. According to the
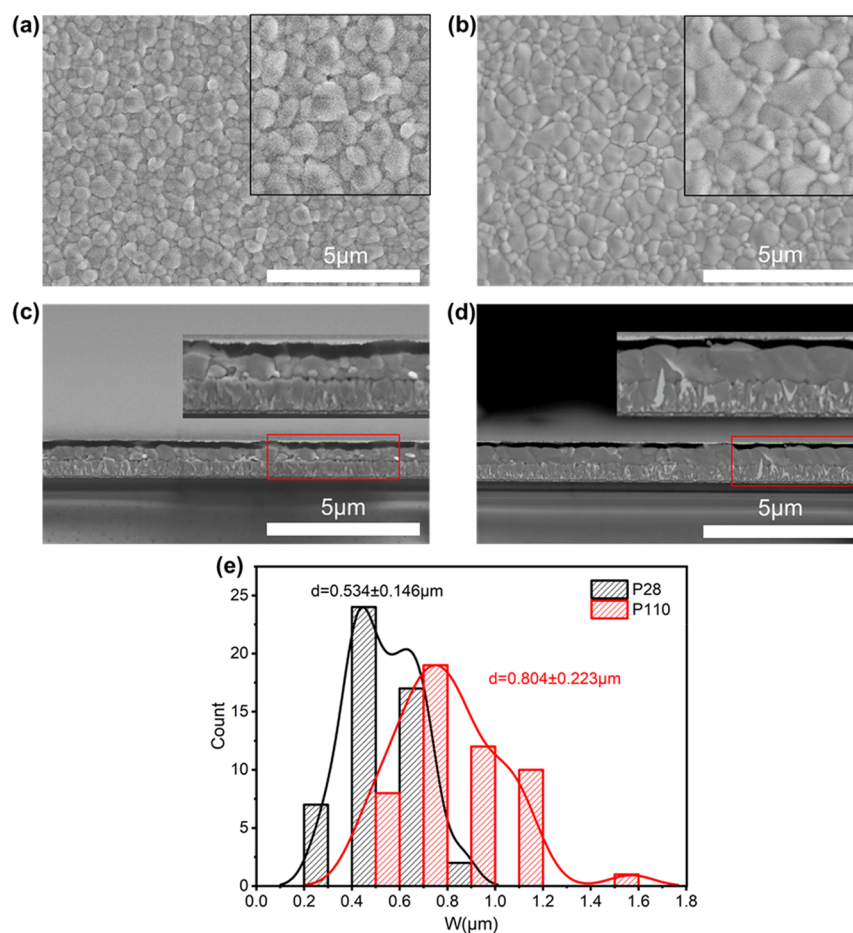
Figure 3. (a) and (b) show SEM images of the morphology of perovskite films P28 and P110, respectively. The insets are high-magnification local enlargements, respectively. (c) and (d) are SEM images of the cross-section morphology of perovskite films P28 and P110, respectively. (e) Grain size distribution of the P28 and P110 perovskite samples.
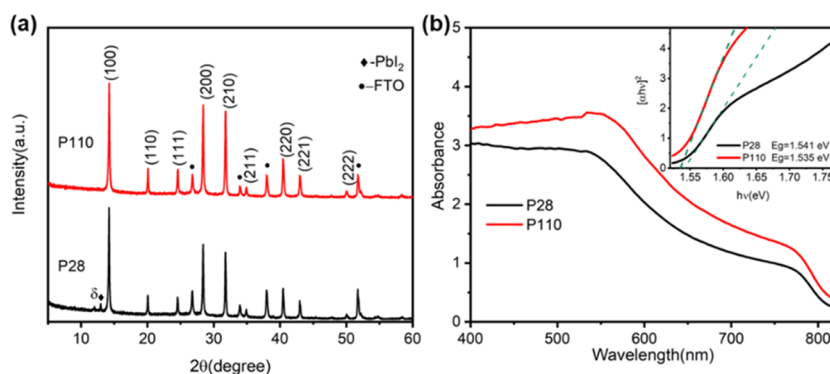

Figure 4. (a) XRD patterns of P28 and P110 perovskite films. (b) UV−vis absorption spectra of P28 and P110 films. The insets show the corresponding Tauc plots of different samples.

comparison of the XRD peak intensity in Figure S3, it is found that the preferential growth orientation of all PbI₂ films moves toward the C (001) axis. Interestingly, the peak intensity increases gradually with the substrate preheating temperature increment from 28 to 110 °C but decreases slightly when the temperature reaches 130 °C. It is noted that the amount of PbI₂ powder for the evaporated layer is almost the same for all samples. Therefore, evaporation of PbI₂ at a relatively high substrate temperature can improve the crystallinity of the film. However, an overall high temperature will cause the reverse evaporation phenomenon of PbI₂, leading to the weakened

main peak intensity of PbI₂. This result is consistent with the conclusion that the thickness of PbI₂ in Figure S1 decreases at 130 °C. By analyzing the morphology of PbI₂ films deposited at different substrate temperatures, the influence of substrate temperature on the growth of PbI₂ crystals was obtained. As shown in Figure 2h, when the substrate is heated, the epitaxial growth of PbI₂ molecules deposited by evaporation is achieved, thus forming a PbI₂ film with high crystallinity and close bonding with the substrate. When the temperature of the substrate is low, the growth of PbI₂ cannot achieve the purpose of epitaxial growth and the formed PbI₂ film has low
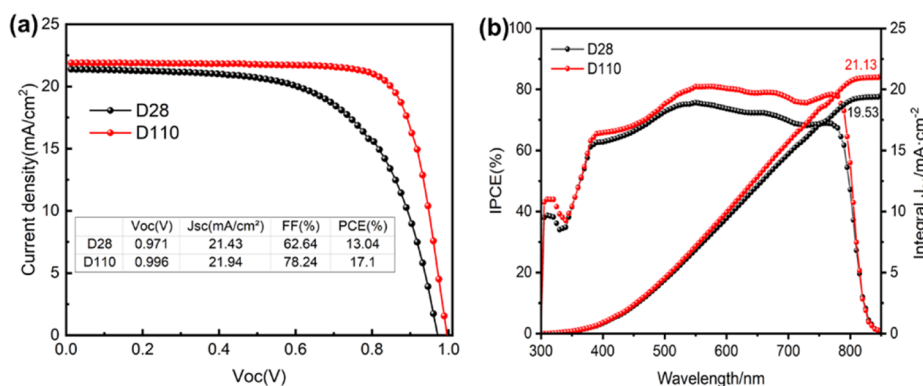
Figure 5. (a) $J{-}V$ curves of D28 and D110. (b) EQE spectra with integrated J_{sc} of D28 and D110.
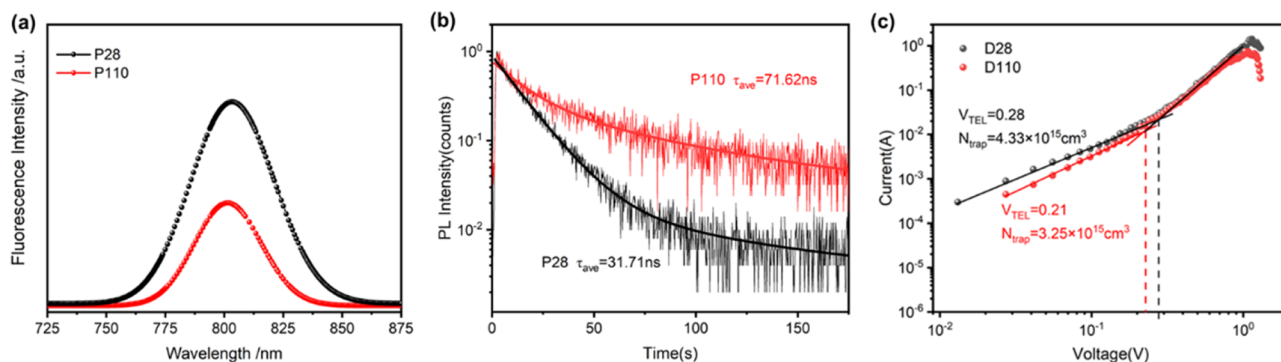

Figure 6. (a) PL spectra of P28 and P110 films. (b) TRPL spectra of P28 and P110 films. (c) SCLC of electron-layer-only devices taking a structure of FTO/TiO_2/perovskite/PCBM/Au.

crystallinity and poor binding with the substrate. These were mutually verified by SEM and XRD diffraction data.

The $CsBr/PbI_2$ precursor film reacted with FAI by VRM to obtain a perovskite absorption layer. Figure 3a and b show the top-view SEM images of perovskite films P28 and P110, respectively. Combined with the grain size distribution diagram in Figure 3e, it was observed that the P28 sample contains pinholes, with a large proportion of small perovskite grains and a rough surface compared to the surface of P110. Figure 3c and d show the cross-section SEM images of the morphology of perovskite films P28 and P110, respectively. It is observed that there are large gaps and holes between the perovskite layer and the electron transport layer in the P28 sample. The perovskite layer in P110 samples was closely bound to the electron transport layer, and the perovskite grains showed columnar growth. The combination of the perovskite layer with the electron transport layer and the growth characteristics of the large grain can improve the transport efficiency of the photogenerated carrier, which is conducive to improving the photoelectric performance of the device.

The influence of different PbI_2 precursors on the crystallization of perovskite films is shown in Figure 4a. The diffraction peaks of all the films are located at 14.36, 20.19, 24.7, 28.51, 31.89, 35.02, 40.55, 43.11, and 50.19°, respectively, corresponding to the (100), (110), (111), (200), (210), (211), (220), (221), and (222) planes of $Cs_xFA_{1-x}PbI_{3-y}Br_y$.[31] In addition, it is observed that there was no peak attributed to PbI_2 in the P110 sample (Figure S4) while the other three samples had an additional peak for each at around 12.9°, attributing to PbI_2. In particular, the strength of PbI_2 in the P130 sample was almost half of the diffraction

strength of perovskite, which is seen in combination with the cross section of the P130 sample in Figure S1c. This is because the PbI_2 film prepared at the substrate temperature of 130 °C is denser, which makes it more difficult for FAI to diffuse to the bottom of PbI_2 to participate in the reaction. Therefore, a large amount of PbI_2 remained in the perovskite film. The UV−vis absorption spectra of samples are shown in Figure 4b. It is seen that the light absorption of the $Cs_xFA_{1-x}PbI_{3-y}Br_y$ film improved with increasing the substrate temperature, which is attributed to the improved crystallization of the P110 sample. In addition, from the inset graph of Figure S5, a slight change in the band gap of $Cs_xFA_{1-x}PbI_{3-y}Br_y$ is observed. By calculation, the band gaps of P28, P90, P110, and P130 were ~1.541, 1.539, 1.535, and 1.539 eV, respectively. In addition, the P110 sample had a smaller band gap and the light absorption of P110 sample was stronger than that of other samples in the range of 570 to 820 nm.

The $J{-}V$ curves of D28 and D110 are shown in Figure 5a. The PCE of D110 is significantly improved to approaching 17.1%, which is much higher than that of D28 (13.04%). The $J{-}V$ curves and photovoltaic parameters of the different perovskite devices are shown in Figure S6 and Table S1, respectively. It is found that the change of substrate temperature can indeed improve the PbI_2 crystallization and improve the photovoltaic performance of the devices. The $Cs_xFA_{1-x}PbI_{3-y}Br_y$ device achieves the champion performance when the PbI_2 film is deposited at 110 °C. In addition, the integrated current density of the EQE of D110 and D28 is 21.13 and 19.53 mA/cm^{-2}, respectively (Figure 5b), which is consistent with the $J{-}V$ results mentioned above.
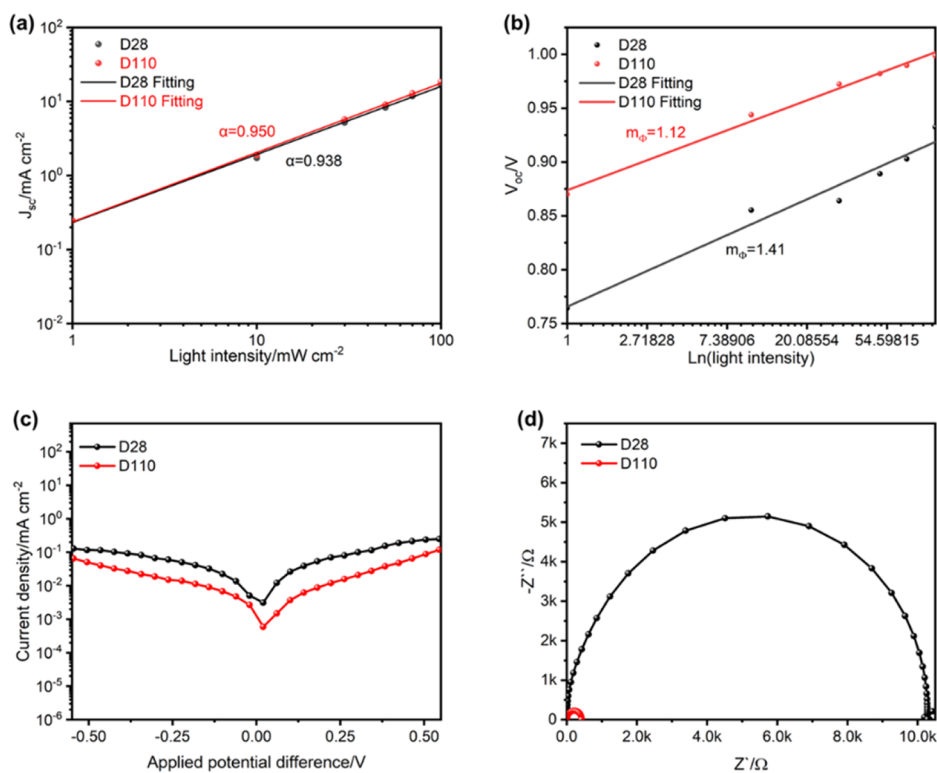
Figure 7. The light intensity of D28 and D110 depends on J_{sc} (a) and V_{oc} (b), dark $J-V$ curve (c), and Nyquist plot (d) when the bias voltage is -1.2 V in dark conditions.

In fact, the acceleration of the charge transfer process inside the device plays an important role in improving the photovoltaic performance of the device. The PL spectra of P28 and P110 films on TiO$_2$/FTO glass are shown in Figure 6a. Compared with the P28 sample, the PL strength of the P110 film is significantly lower, and Figure S7 also shows that the PL strength of P110 is lower than those of the other three samples. The TR-PL spectra of P28 and P110 films are shown in Figure 6b, and the TR-PL decay curves are fitted by a bi-exponential equation as follows:[32] $I(t) = \sum_i A_i \exp(-t/\tau_i)$, where A_i is the decay amplitude and τ_i is the decay time. The average PL decay time (τ_{ave}) is calculated with the fitted A_i and τ_i values as follows:[33] $\tau_{ave} = \frac{\sum A_i \tau_i^2}{\sum A_i \tau_i}$; the relevant parameters are listed in Table S2. The fast decay life (τ_1) is the surface non-radiative recombination, and the slow decay life (τ_2) represents the bulk recombination. Compared with the τ_{ave} (31.7 ns) of P28, the τ_{ave} (71.62 ns) of P110 significantly increases, which indicates that the trap state of P110 decreased, indicating that P110 has excellent charge transfer performance.[34] To evaluate the influence of PbI$_2$ prepared at different substrate temperatures on the defect-state density of perovskite films, we measured the SCLC of the related perovskite devices. As shown in Figure 6c, the trap-state density (N_{trap}) was determined by the trap filling limit voltage (V_{TEL}) according to the formula[35] $V_{TEL} = \frac{eL^2 N_{trap}}{2\varepsilon\varepsilon_0}$ (L is the thickness of the perovskite film, $\varepsilon = 35$ is the perovskite relative dielectric constant, $\varepsilon_0 = 8.854 \times 10^{-12}$ F/m is the vacuum dielectric constant, V_{TEL} is the starting voltage of the trap filling limit, and e is the basic charge of the electron 1.60×10^{-19} C). The N_{trap} of P110 (3.25×10^{15} cm^3) is significantly lower than that

of P28 (4.33×10^{15} cm^3), which is consistent with the results of PL and TRPL.

To investigate the charge recombination kinetics, the light intensity-dependent J_{sc} and V_{oc}, dark $J-V$ curves, and Nyquist plots of D28 and D110 were measured, as shown in Figure 7. The light intensity-dependent J_{sc} (Figure 7a) data were fitted using the equation $J_{sc} \propto I^\alpha$ (α represents the slope of the curve).[36] The calculated slopes (α) of D28 and D110 were 0.938 and 0.950, respectively. Obviously, the α of D110 is closer to the standard value ($\alpha = 1$) than that of D28, which means that D110 had lower charge recombination and lower charge loss during the photoelectric conversion. In addition, the logarithmic plot of the open-circuit voltage V_{oc} and the light intensity I (Figure 7b) was fitted linearly by the equation[36] $V_{oc} = \frac{m_\Phi kT}{q}\ln\Phi_{ph}$ (Φ is the incident light intensity, q is the basic charge, k is Boltzmann's constant, T is the absolute temperature, and m_Φ is the ideal factor). The calculated m_Φ values of D28 and D110 are 1.41 and 1.12, respectively. The smaller m_Φ value of D110 verifies that the trap-assisted radiation-free recombination is limited compared with D28. According to the dark $J-V$ curve (Figure 7c), it is found that the current density of D110 is lower than that of D28 in the voltage range of -0.5–0.5 V, which means that D110 has lower charge recombination and less charge loss in the photoelectric conversion process.[37] The samples were tested by electrochemical impedance spectroscopy (EIS) under dark conditions with a bias voltage of -1.2 V; the results are shown in Figure 7d, and the equivalent circuit model is shown in Figure S8, including compound resistance (R_{rec}), series resistance (R_s), and contact resistance (R_{co}).[38,39] The Nyquist plots of D28 and D110 show a semicircle in the high-frequency region. The high-frequency half-circle is related to charge
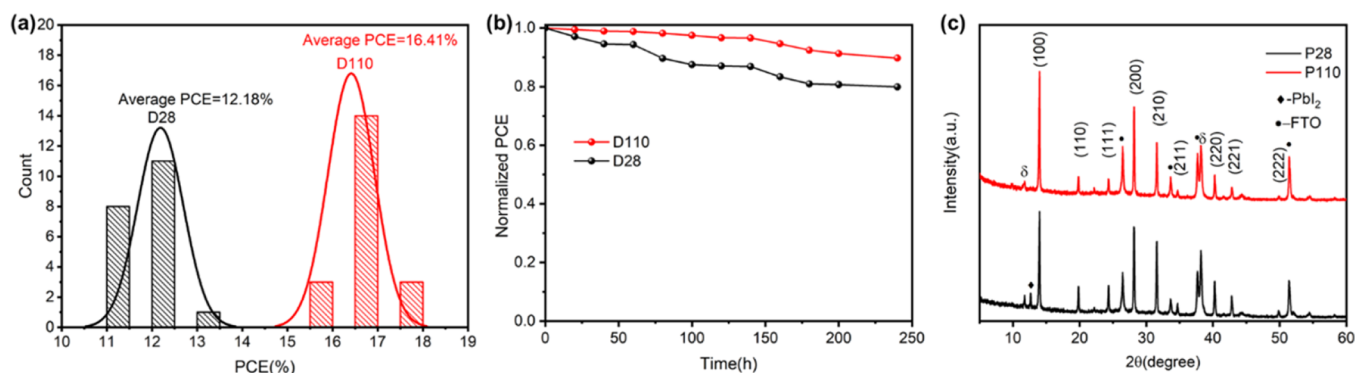
Figure 8. (a) Statistical distribution of PCE of D28 and D110. (b) The PCE of the device changes with time at 50% RH and 25 °C air conditions. (c) XRD patterns of P28 and P110 after 240 h storage.

transfer and transfer resistance. Clearly, D110 has a lower contact resistance compared to that of D28, which indicates that the dark recombination in the latter device is effectively reduced.

Figure 8a shows the normal distribution of 20 PCE data of D28 and D110. It is found that the average PCEs of D110 and D28 are 16.41 and 12.18%, respectively. In addition, to study the environmental stability of the device, we stored the device at a relative humidity of 50% without any packaging conditions and monitored its PCE within 240 h. Figure 8b shows that the PCE of D28 decreases by about 16% while the PCE of D110 decreases by only about 9.4%. In order to study the reason of PCE reduction, we carried out an XRD test on the device. As shown in Figure 8c, it is found that both P28 and P110 have a certain degree of phase transition, with the appearance of the δ phase diffraction peak. However, an obvious PbI_2 peak appears in the diffraction pattern of P28, indicating the decomposition of the perovskite. This result shows that the P110 sample has an enhanced operational stability in the ambient air.

4. CONCLUSIONS

In summary, the $CsBr/PbI_2$ precursor that is adjusted by substrate heating temperature has an obviously active effect on fabrication of high-quality perovskite thin films by VRM. $CsBr/PbI_2$ films prepared at 110 °C show the highest crystallinity. The perovskite thin film prepared by this protocol exhibits an improved surface with large grain size, few pinholes, and low radiation recombination. The fabricated solar cell device has a champion efficiency of 17.1% and exhibits an excellent operational stability. Therefore, substrate preheating can obtain high-quality PbI_2 precursor films, which is an effective method to prepare high-performance perovskite films by VRM technology. This method provides an effective strategy for preparation of large-area and high-performance PSCs.

■ ASSOCIATED CONTENT

Ⓢ Supporting Information

The Supporting Information is available free of charge at https://pubs.acs.org/doi/10.1021/acsomega.3c00318.

Grain size distribution diagram of lead iodide; XRD patterns of the $CsBr/PbI_2$ film at substrate temperatures of 28, 90, 110, and 130°C; XRD patterns of P28, P90, P110, and P130 films; UV−vis absorption spectra of P28, P90, P110, and P130 films; $J−V$ curves of D28, D90, D110, and D130; PL spectra of P28, P90, P110,

and P130; equivalent circuit models; PV parameters of different samples; TRPL key parameters of the P28 and P110 (PDF)

■ AUTHOR INFORMATION

Corresponding Authors

Guoyuan Zheng − *Guangxi Key Laboratory of Optical and Electronic Material and Devices, School of Materials Science and Engineering, Guilin University of Technology, Guilin, Guangxi 541004, China;* ⓞ orcid.org/0000-0002-0033-8314; Email: zhengguoyuan@glut.edu.cn

Fei Long − *Guangxi Key Laboratory of Optical and Electronic Material and Devices, School of Materials Science and Engineering and Collaborative Innovation Center for Exploration of Nonferrous Metal Deposits and Efficient Utilization of Resources, Guilin University of Technology, Guilin, Guangxi 541004, China;* Email: longf@glut.edu.cn

Authors

Qin Zou − *Guangxi Key Laboratory of Optical and Electronic Material and Devices, School of Materials Science and Engineering, Guilin University of Technology, Guilin, Guangxi 541004, China*

Disheng Yao − *Guangxi Key Laboratory of Optical and Electronic Material and Devices, School of Materials Science and Engineering, Guilin University of Technology, Guilin, Guangxi 541004, China*

Jilin Wang − *Guangxi Key Laboratory of Optical and Electronic Material and Devices, School of Materials Science and Engineering and Collaborative Innovation Center for Exploration of Nonferrous Metal Deposits and Efficient Utilization of Resources, Guilin University of Technology, Guilin, Guangxi 541004, China;* ⓞ orcid.org/0000-0001-6381-7438

Nan Tian − *Guangxi Key Laboratory of Optical and Electronic Material and Devices, School of Materials Science and Engineering, Guilin University of Technology, Guilin, Guangxi 541004, China;* ⓞ orcid.org/0000-0002-1423-7581

Shuyi Mo − *Guangxi Key Laboratory of Optical and Electronic Material and Devices, School of Materials Science and Engineering, Guilin University of Technology, Guilin, Guangxi 541004, China*

Complete contact information is available at:
https://pubs.acs.org/10.1021/acsomega.3c00318

Notes

■ ACKNOWLEDGMENTS

■ REFERENCES

(1) Lin, D.; Zhan, Z.; Huang, X.; Liu, P.; Xie, W. Advances in components engineering in vapor deposited perovskite thin film for photovoltaic application. *Materials Today Advances* **2022**, *16*, No. 100277.

(2) Zhao, J.; Deng, Y.; Wei, H.; Zheng, X.; Yu, Z.; Shao, Y.; Shield, J. E.; Huang, J. Strained hybrid perovskite thin films and their impact on the intrinsic stability of perovskite solar cells. *Sci. Adv.* **2017**, *3*, eaao5616.

(3) Liu, J.; Shi, B.; Xu, Q.; Li, Y.; Chen, B.; Wang, Q.; Wang, P.; Zhao, Y.; Zhang, X. Crystalline quality control in sequential vapor deposited perovskite film toward high efficiency and large scale solar cells. *Sol. Energy Mater. Sol. Cells* **2021**, *233*, No. 111382.

(4) Saikia, D.; Betal, A.; Bera, J.; Sahu, S. Progress and challenges of halide perovskite-based solar cell- a brief review. *Mater. Sci. Semicond. Process.* **2022**, *150*, No. 106953.

(5) *Nest Research-Cell Efficiency Chart*. <https://www.nrel.gov/pv/cell-efficiency.html> (accessed November 20, 2022).

(6) Yantara, N.; Sabba, D.; Yanan, F.; Kadro, J. M.; Moehl, T.; Boix, P. P.; Mhaisalkar, S.; Grätzel, M.; Grätzel, C. Loading of mesoporous titania films by $CH_3NH_3PbI_3$ perovskite, single step vs. sequential deposition. *Chem. Commun.* **2015**, *51*, 4603–4606.

(7) Im, J.-H.; Kim, H.-S.; Park, N.-G. Morphology-photovoltaic property correlation in perovskite solar cells: One-step versus two-step deposition of $CH_3NH_3PbI_3$. *APL Mater.* **2014**, *2*, No. 081510.

(8) Zhang, T.; Guo, N.; Li, G.; Qian, X.; Li, L.; Zhao, Y. A general non-CH_3NH_3X (X = I, Br) one-step deposition of $CH_3NH_3PbX_3$ perovskite for high performance solar cells. *J. Mater. Chem. A* **2016**, *4*, 3245–3248.

(9) Ghosh, J.; Natu, G.; Giri, P. K. Plasmonic hole-transport-layer enabled self-powered hybrid perovskite photodetector using a modified perovskite deposition method in ambient air. *Org. Electron.* **2019**, *71*, 175–184.

(10) Jeon, N. J.; Noh, J. H.; Kim, Y. C.; Yang, W. S.; Ryu, S.; Seok, S. I. Solvent engineering for high-performance inorganic-organic hybrid perovskite solar cells. *Nat. Mater.* **2014**, *13*, 897–903.

(11) Moreno-Romero, P. M.; Corpus-Mendoza, A. N.; Millán-Franco, M. A.; Rodríguez-Castañeda, C. A.; Torres-Herrera, D. M.; Liu, F.; Hu, H. Roughness and structural modification of PbI_2 thin films by isopropanol treatment to improve methylammonium lead halide formation and solar cell efficiency. *J. Mater. Sci.: Mater. Electron.* **2019**, *30*, 17491–17503.

(12) Zhang, J.; Zhang, L.; Li, X.; Zhu, X.; Yu, J.; Fan, K. Binary Solvent Engineering for High-Performance Two-Dimensional Perovskite Solar Cells. *ACS Sustainable Chem. Eng.* **2019**, *7*, 3487–3495.

(13) Dhamaniya, B. P.; Chhillar, P.; Kumar, A.; Chandratre, K.; Mahato, S.; Ganesan, K. P.; Pathak, S. K. Orientation-Controlled (h 0 l) PbI_2 Crystallites Using a Novel Pb–Precursor for Facile and Quick Sequential MAPbI3 Perovskite Deposition. *ACS Omega* **2020**, *5*, 31180–31191.

(14) Tavakoli, M. M.; Yadav, P.; Prochowicz, D.; Sponseller, M.; Osherov, A.; Bulović, V.; Kong, J. Controllable Perovskite Crystallization via Antisolvent Technique Using Chloride Additives for Highly Efficient Planar Perovskite Solar Cells. *Adv. Energy Mater.* **2019**, *9*, 1803587.

(15) Prochowicz, D.; Tavakoli, M. M.; Solanki, A.; Goh, T. W.; Pandey, K.; Sum, T. C.; Saliba, M.; Yadav, P. Understanding the effect of chlorobenzene and isopropanol anti-solvent treatments on the recombination and interfacial charge accumulation in efficient planar perovskite solar cells. *J. Mater. Chem. A* **2018**, *6*, 14307–14314.

(16) Zhang, B.; Liu, D.; Chen, P.; Liu, W.; Zhao, J.; Li, H.; Liu, H. Improved perovskite crystallization via antisolvent-assisted processed using additive engineering for efficient perovskite solar cells. *J. Alloys Compd.* **2021**, *855*, No. 157396.

(17) Zhang, P.; Cao, F.; Tian, W.; Li, L. Thiamine additive engineering enables improved film formation towards high efficiency and moisture stability in perovskite solar cells. *Sci. China Mater.* **2021**, *65*, 321–327.

(18) Ávila, J.; Momblona, C.; Boix, P. P.; Sessolo, M.; Bolink, H. J. Vapor-Deposited Perovskites: The Route to High-Performance Solar Cell Production? *Joule* **2017**, *1*, 431–442.

(19) Luo, L.; Zhang, Y.; Chai, N.; Deng, X.; Zhong, J.; Huang, F.; Peng, Y.; Ku, Z.; Cheng, Y.-B. Large-area perovskite solar cells with $Cs_xFA_{1-x}PbI_{3-y}Br_y$ thin films deposited by a vapor–solid reaction method. *J. Mater. Chem. A* **2018**, *6*, 21143–21148.

(20) Jiang, Y.; Leyden, M. R.; Qiu, L.; Wang, S.; Ono, L. K.; Wu, Z.; Juarez-Perez, E. J.; Qi, Y. Combination of Hybrid CVD and Cation Exchange for Upscaling Cs-Substituted Mixed Cation Perovskite Solar Cells with High Efficiency and Stability. *Adv. Funct. Mater.* **2018**, *28*, 1703835.

(21) Chen, X.; Cao, H.; Yu, H.; Zhu, H.; Zhou, H.; Yang, L.; Yin, S. Large-area, high-quality organic–inorganic hybrid perovskite thin films via a controlled vapor–solid reaction. *J. Mater. Chem. A* **2016**, *4*, 9124–9132.

(22) Liu, M.; Johnston, M. B.; Snaith, H. J. Efficient planar heterojunction perovskite solar cells by vapour deposition. *Nature* **2013**, *501*, 395–398.

(23) Abbas, H. A.; Kottokkaran, R.; Ganapathy, B.; Samiee, M.; Zhang, L.; Kitahara, A.; Noack, M.; Dalal, V. L. High efficiency sequentially vapor grown n-i-p $CH_3NH_3PbI_3$ perovskite solar cells with undoped P3HT as p-type heterojunction layer. *APL Mater.* **2015**, *3*, No. 016105.

(24) Chen, C.-W.; Kang, H.-W.; Hsiao, S.-Y.; Yang, P.-F.; Chiang, K.-M.; Lin, H.-W. Efficient and uniform planar-type perovskite solar cells by simple sequential vacuum deposition. *Adv. Mater.* **2014**, *26*, 6647–6652.

(25) Longo, G.; Gil-Escrig, L.; Degen, M. J.; Sessolo, M.; Bolink, H. J. Perovskite solar cells prepared by flash evaporation. *Chem. Commun.* **2015**, *51*, 7376–7378.

(26) Borchert, J.; Milot, R. L.; Patel, J. B.; Davies, C. L.; Wright, A. D.; Maestro, L. M.; SnaithOrcid, H. J.; HerzOrcid, L. M.; Johnston, M. B. Large-Area, Highly Uniform Evaporated Formamidinium Lead Triiodide Thin Films for Solar Cells. *ACS Energy Lett.* **2017**, *2*, 2799–2804.

(27) Gil-Escrig, L.; Momblona, C.; La-Placa, M-G.; Boix, P. P.; Sessolo, M.; Bolink, H. J. Vacuum Deposited Triple-Cation Mixed-Halide Perovskite Solar Cells. *Adv. Energy Mater.* **2018**, *8*, 1703506.

(28) Tong, G.; Li, H.; Li, G.; Zhang, T.; Li, C.; Yu, L.; Xu, J.; Jiang, Y.; Shi, Y.; Chen, K. Mixed cation perovskite solar cells by stack-sequence chemical vapor deposition with self-passivation and gradient absorption layer. *Nano Energy* **2018**, *48*, 536–542.

(29) Wang, S.; Tan, L.; Zhou, J.; Li, M.; Zhao, X.; Li, H.; Tress, W.; Ding, L.; Graetzel, M.; Yi, C. Over 24% efficient MA-free $Cs_xFA_{1-x}PbX_3$ perovskite solar cells. *Joule* **2022**, *6*, 1344–1356.

(30) Abdulnabi, R. K.; Mohsin, M. H.; Ismail, R. A.; Mousa, A. M.; Jawad, M. F. Effect of laser energy on the properties of nanostructured lead iodide film prepared via pulsed laser deposition technique. *Optik* **2019**, *176*, 206–213.

(31) Deng, Y.; Xu, S.; Chen, S.; Xiao, X.; Zhao, J.; Huang, J. Defect compensation in formamidinium–caesium perovskites for highly efficient solar mini-modules with improved photostability. *Nat. Energy* **2021**, *6*, 633–641.

(32) Yang, D.; Yang, R.; Ren, X.; Zhu, X.; Yang, Z.; Li, C.; Liu, S. Hysteresis-suppressed high-efficiency flexible perovskite solar cells using solid-state ionic-liquids for effective electron transport. *Adv. Mater.* **2016**, *28*, 5206−5213.

(33) Tu, Y.; Yang, X.; Su, R.; Luo, D.; Cao, Y.; Zhao, L.; Liu, T.; Yang, W.; Zhang, Y.; Xu, Z.; Liu, Q.; Wu, J.; Gong, Q.; Mo, F.; Zhu, R. Diboron-assisted interfacial defect control strategy for highly efficient planar perovskite solar cells. *Adv. Mater.* **2018**, *30*, 1805085.

(34) Chen, Q.; Zhou, H.; Song, T.-B.; Luo, S.; Hong, Z.; Duan, H.-S.; Dou, L.; Liu, Y.; Yang, Y. Controllable Self-Induced Passivation of Hybrid Lead Iodide Perovskites toward High Performance Solar Cells. *Nano Lett.* **2014**, *14*, 4158−4163.

(35) Wang, D.; Li, W.; Sun, W.; Liu, X.; Li, G.; Wu, Z.; Wu, J.; Lan, Z. Guanidinium iodide modification enabled highly efficient and stable all-inorganic $CsPbBr_3$ perovskite solar cells. *Electrochim. Acta* **2021**, *365*, No. 137360.

(36) Cowan, S. R.; Roy, A.; Heeger, A. J. Recombination in polymer-fullerene bulk heterojunction solar cells. *Phys. Rev. B* **2010**, *82*, No. 245207.

(37) Liu, T.; Jiang, Y.; Qin, M.; Liu, J.; Sun, L.; Qin, F.; Hu, L.; Xiong, S.; Jiang, X.; Jiang, F.; Peng, P.; Jin, S.; Lu, X.; Zhou, Y. Tailoring vertical phase distribution of quasi-two-dimensional perovskite films via surface modification of hole-transporting layer. *Nat. Commun.* **2019**, *10*, 1−10.

(38) Yang, J.; Chen, Y.; Tang, W.; Wang, S.; Ma, Q.; Wu, Y.; Yuan, N.; Ding, J.; Zhang, W.-H. Crystallization tailoring of cesium/formamidinium double-cation perovskite for efficient and highly stable solar cells. *J. Energy Chem.* **2020**, *48*, 217−225.

(39) Hu, Z.; An, Q.; Xiang, H.; Aigouy, L.; Sun, B.; Vaynzof, Y.; Chen, Z. Enhancing the Efficiency and Stability of Triple-Cation Perovskite Solar Cells by Eliminating Excess PbI_2 from the Perovskite/Hole Transport Layer Interface. *ACS Appl. Mater. Interfaces* **2020**, *12*, 54824−54832.